

Article

Metal Exchangeability in the REE-Enriched Biogenic Mn Oxide Birnessite from Ytterby, Sweden

Bert Allard ^{1,*}, Susanne Sjöberg ², Viktor Sjöberg ¹ , Henrik Skogby ³  and Stefan Karlsson ¹¹ Man-Technology-Environment Research Centre (MTM), Örebro University, SE-701 82 Örebro, Sweden² Department of Geological Sciences, Stockholm University, SE-106 91 Stockholm, Sweden³ Department of Geosciences, Swedish Museum of Natural History, SE-114 18 Stockholm, Sweden

* Correspondence: bert.allard@oru.se; Tel.: +46-(70)-69-30-595

Abstract: A black substance exuding from fractures was observed in 2012 in Ytterby mine, Sweden, and identified in 2017 as birnessite with the composition $M_x[Mn(III,IV)]_2O_4 \cdot (H_2O)_n$. M is usually calcium and sodium, with x around 0.5. The Ytterby birnessite is unique, with M being calcium, magnesium, and also rare earth elements (REEs) constituting up to 2% of the total metal content. The biogenic origin of the birnessite was established in 2018. Analysis of the microbial processes leading to the birnessite formation and the REE enrichment has continued since then. The process is fast and dynamic, as indicated by the depletion of manganese and of REE and other metals in the fracture water during the passage over the precipitation zone in the mine tunnel. Studies of the exchangeability of metals in the structure are the main objective of the present program. Exposure to solutions of sodium, calcium, lanthanum, and iron led to exchanges and altered distribution of the metals in the birnessite, however, generating phases with almost identical structures after the exchanges, and no new mineral phases were detected. Exchangeability was more efficient for trivalent elements (REE) over divalent (calcium) and monovalent (sodium) elements of a similar size (ionic radii 90–100 pm).

Keywords: Ytterby mine; biogenic Mn mineralization; birnessite; rare earth elements enrichment

Citation: Allard, B.; Sjöberg, S.; Sjöberg, V.; Skogby, H.; Karlsson, S. Metal Exchangeability in the REE-Enriched Biogenic Mn Oxide Birnessite from Ytterby, Sweden. *Minerals* **2023**, *13*, 1023. <https://doi.org/10.3390/min13081023>

Academic Editors: Anna Panyushkina and Maxim Muravyov

Received: 30 June 2023

Revised: 25 July 2023

Accepted: 29 July 2023

Published: 30 July 2023



Copyright: © 2023 by the authors. Licensee MDPI, Basel, Switzerland. This article is an open access article distributed under the terms and conditions of the Creative Commons Attribution (CC BY) license (<https://creativecommons.org/licenses/by/4.0/>).

1. Introduction

The Ytterby mine in Sweden is known for the discovery of five rare earth elements (REEs), as well as scandium, yttrium, and tantalum. The mine is located on Resarö Island in the Baltic Sea, some 20 km NE of Stockholm. The site, which is described in detail by Sjöberg et al. [1] (geologic setting, hydrology), belongs to the Proterozoic Svecofennian domain, which covers most of the northern and central part of Sweden. The mine is located in a pegmatite body, which is bordered by amphibolite in the NW and by gneiss in the SE. The Ytterby pegmatite belongs to the NYF family, which is enriched in niobium, yttrium, and fluorine. The average hydraulic conductivity in the bedrock around the mine has been estimated to be around 3×10^6 m/sec. That would correspond to an inflow of water to the mine shaft of some 9 m³/day. Some 50 minerals have been identified in the mine, including 15 containing REE [2,3].

The mine was closed in 1933, after 170 years of mining for quartz and feldspar. The mine shaft was used as a fuel deposit from the 1950s until 1995. During this period, the shaft was covered, and a tunnel was opened through the bedrock into the shaft.

In 2012, a black substance was discovered in the opening of a water-bearing fracture in the tunnel wall, Figures 1 and 2, and a program for identification started. The composition of the substance (here denoted YBS) was determined from elemental analysis, as well as XRD and SEM with EDS. The YBS was identified as a manganese oxide of the birnessite type, ideally $M_{0.5}[Mn(III,IV)]_2O_4 \cdot (H_2O)_n$, where M usually is sodium or calcium (mindat, 2019) [4]. Birnessite was discovered and defined as a new mineral phase in 1956 [5], and

there are numerous reported studies of natural birnessite [6–16], as well as of synthetic birnessite, since then, in most cases on the adsorption properties and structure [17–38]. There are also a few reported observations of birnessite that has precipitated on rock walls in tunnels and caves, similar to the Ytterby birnessite [39–41].



Figure 1. Ytterby mine on Resarö Island. Map showing the major YBS sampling location.



Figure 2. YBS with gas bubbles on the tunnel wall beneath the opening of a water-bearing fracture.

What makes the Ytterby birnessite unique is the enrichment of yttrium and REE, corresponding to up to 2% of the total metal content and replacing primarily sodium in the structure. The elemental composition and phase analysis are described in Sjöberg et al. (2017) [1]. Analysis of the organics, including IR and EPR spectroscopy, indicated that there was ca. 1% organic matter (lipids) associated with the YBS, and a biogenic origin was assumed. The microbial community inhabiting the YBS was characterized, known manganese oxidizers were identified, and the biogenic origin of the YBS was analyzed and verified [42–45]. The results revealed a startling bacterial diversity, and a model for microbe-mediated oxidation of manganese and the formation of birnessite was proposed [46]. The model was based on detailed studies and characterization of the microbial community that apparently is active in the process.

The objective of the present phase of the project is further studies of the processes leading to formation of the REE-enriched birnessite in the Ytterby mine tunnel. The

exchangeability of the metals corresponding to M in the YBS birnessite phase (sodium, calcium, REE, etc.) is studied in particular.

2. Materials and Methods

2.1. Sampling of YBS and Fracture Water

The solid precipitate (YBS) was collected in the opening of a major water-bearing fracture in the wall of the tunnel leading into the mine shaft. The YBS sample was dried at ca. 30 °C until constant weight (dry weight), followed by washing with deionized water (18.2 MΩ) and then drying once more.

Water that was trickling out from the fracture was sampled above and below the YBS precipitation zone (cf. Figures 1 and 2) on the same day as the sampling of the precipitate and was filtered onsite (PP membrane filters, 0.20 mm pore diameter) and stored in polyethylene bottles. Temperature, electric conductivity, and pH were measured in the field. Samples for element analysis (ICP-MS) were acidified (HNO₃) and stored in a fridge until analysis.

2.2. Characterization and Analysis of YBS

2.2.1. Environmental Scanning Electron Microscopy (ESEM-EDS)

Scanning electron microscopy was carried out using a Quanta environmental scanning electron microscope (ESEM). An energy-dispersive X-ray spectrometer (EDS) was used for compositional information.

2.2.2. Sequential Washing

A sequential washing procedure was designed for separation and removal of organics and ion exchangeable and adsorbed ions, as well as fresh hydroxides and oxyhydroxides and any suspended mineral grains from the original YBS sample (denoted YBS_{Nat}). The three steps in sequence (L/S = 10, 24 h each step C1 and C2; 1 h step C3) are:

- C1 Organics, dichloromethane/methanol (CH₂Cl₂/CH₃OH) 1:1; 2 times
- C2 Exchangeable ions, 0.11 M acetic acid (CH₃COOH, HAc), pH 4.2
- C3 Suspended colloids, deionized water (18.2 MΩ); 3 times

The slurry after step C3 (water with the YBS grains, as well as suspended fine particles and colloidal matter) was left to settle for 1 min, and then the water phase with suspended material was discharged. The remaining solid was dried at 30 °C until constant weight.

2.2.3. Element Exchange

The washed YBS_{Nat} sample (denoted YBS_{Red}) was divided into four fractions that were mixed with salt solutions and left for 48 h before separation (centrifugation), followed by washing and drying. The solutions were (1 mol/L) NaNO₃, Ca(NO₃)₂, and La(NO₃)₃, as well as Fe(NO₃)₃ for a sample already exposed to Ca(NO₃)₂. All of the YBS samples were washed 2 times with deionized water after the exposure, prior to the characterization of the element composition (see below) and phases (XRD).

2.2.4. X-ray Diffractometry

Mineral phases were determined by XRD (PANalytical X'Pert-Pro diffractometer, Malvern, Bristol, UK, equipped with X'celerator silicon strip detector and spinning sample holder; CuKα radiation from 5° to 70° 2θ with a step size of 0010° 2θ at 40 mA and 45 kV). The diffraction patterns were analyzed using PANalytical High Score Plus software connected to the Inorganic Crystal Structure Database (CSD), 2017 Version.

2.2.5. IR Spectroscopy

Infrared spectra were recorded on solid YBS samples (PerkinElmer Fourier-Transform Infrared (FT-IR) Spectrum Two, Perkin Elmer, Fairfield, US). The spectra were analyzed using the PerkinElmer Infrared Spectrum software that was provided with the instrument.

2.2.6. Element Analysis

The YBS samples (original, YBS_{Nat} , as well as after washing, YBS_{Red} , and after element exchange, YBS_{Na} , YBS_{Ca} , YBS_{Fe} , YBS_{La}) were analyzed with respect to element composition. The samples (3–3.5 g single samples) were dissolved in conc. HNO_3/HCl (Aqua Regia, Pro Analyti, microwave-assisted digestion), and the solutions were filtered (0.20 μm) prior to analysis by ICP-MS (see below).

2.3. Analysis of Water

Elements were analyzed (fracture waters, washing solutions) by ICP-MS (Agilent 7500), following an established standard procedure (choice of internal standard, reference solutions, etc. [1]); anions by ion chromatography (Metrohm); and carbonate/bicarbonate by titration of total alkalinity (also dissolved organic carbon by DOC-analyzer; Schimadzu TOC-V CPH), following standard procedures [1].

3. Results and Discussion

3.1. Environmental Scanning Electron Microscopy (ESEM-EDS)

ESEM analyses of YBS have previously been presented and discussed [1]. Only one example is presented here—on the composition of the YBS precipitate (YBS_{Nat}) prior to washing and element exchange (Figure 3). The sample was fine-grained and evidently contained suspended crystalline mineral fractions (silicates), but also amorphous metal phases and organics (lipids), according to the previous studies [1].

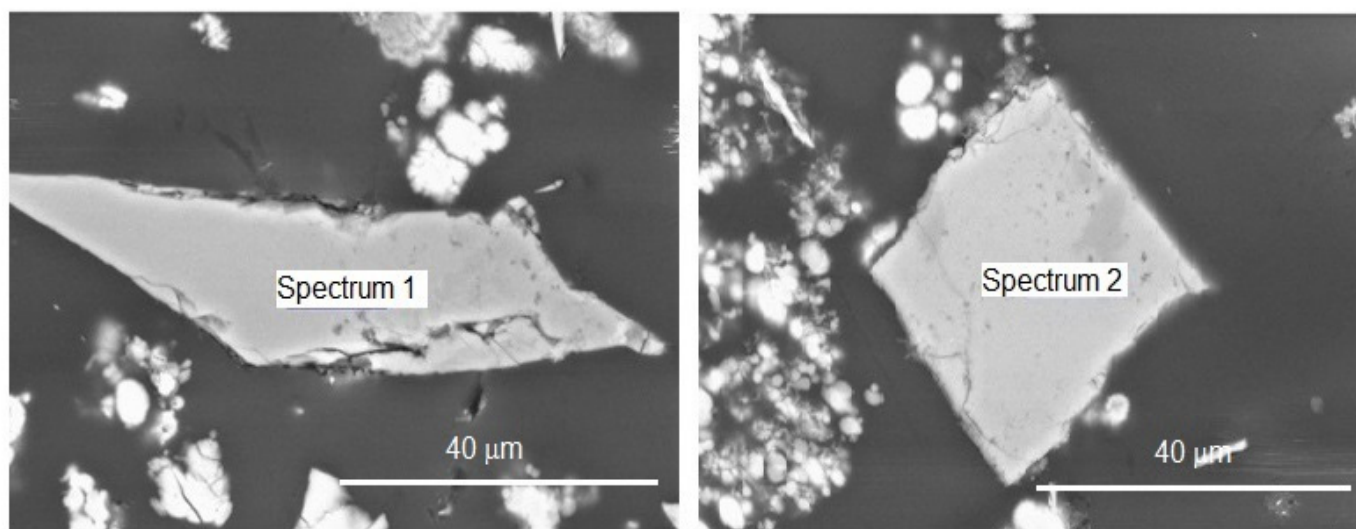


Figure 3. ESEM images showing grains of silicates (feldspars) in YBS samples prior to washing and exposure to salt solutions (examples). Spectrum 1: $\text{Ca}_{0.24}\text{Na}_{0.54}\text{Al}_{1.00}\text{Si}_{1.98}\text{O}_6$; Spectrum 2: $\text{K}_{0.69}\text{Al}_{0.75}\text{Si}_{2.27}\text{O}_6$.

3.2. Fracture Water Chemistry and YBS Metal Enrichment

The composition of the YBS precipitate (YBS_{Nat}) and the fracture water above (Aq_A) and below (Aq_B) the precipitation zone are given in Table 1, as well as the concentration ratio of the fracture waters ($[\text{Aq}_B]/[\text{Aq}_A]$) and an enrichment factor k_e , defined as $[\text{YBS}_{\text{Nat}}]/[\text{Aq}_A]$. Concentration levels of the major components were slightly lower in Aq_B than in Aq_A , except for calcium, carbonate, and sulphate with higher levels in Aq_B . This may reflect some interaction with the rock during the passage over the precipitation zone, where the calcium and carbonate levels may reach saturation, indicating the presence of solid calcium carbonate, considering the $\text{CaCO}_3(\text{s})$ solubility product 3.3×10^{-9} [47].

Table 1. Components in YBS_{Nat} with concentrations above 200 mg/kg, plus all REEs and excluding C, O, and Si concentrations in the fracture water above (Aq_A) and below (Aq_B) the precipitation zone, and the enrichment factor k_e defined as the [YBS_{Nat}]/[Aq_A] ratio.

Element	YBS _{Nat} mg/kg	Aq _A µg/L	Aq _B µg/L	[Aq _B]/[Aq _A]	log k _e L/kg
pH		8.31	8.33		
Cl ⁻		20,900	20,700	0.99	
SO ₄ ²⁻		29,100	35,000	1.20	
HCO ₃ ⁻		205,000	228,000	1.11	
Mn(III,IV)	452,710	172	2.72	0.016	6.42
M(I)					
Na	399	24,510	24,080	0.98	1.21
K	666	1720	1690	0.98	2.59
M(II)					
Ca	64,170	56,360	61,740	1.09	3.06
Mg	4075	8340	8140	0.98	2.69
Ba	1765	4.50	4.17	0.93	5.59
Cu	1555	3.89	3.40	0.87	5.60
Sr	639	250	237	0.95	3.41
Zn	276	0.75	0.65	0.87	5.57
M(III)					
Y	1357	5.00	4.08	0.82	5.43
Al	841	5.26	5.14	0.98	5.20
V	683	2.68	1.82	0.68	5.41
Fe	583	0.40	0.044	0.11	6.16
REE					
Ce	3180	1.15	0.059	0.051	6.44
La	1825	1.04	0.47	0.45	6.24
Nd	1785	1.27	0.69	0.54	6.14
Gd	419	0.44	0.31	0.70	5.98
Pr	418	0.25	0.13	0.52	6.22
Sm	375	0.27	0.18	0.67	6.14
Dy	308	0.43	0.33	0.77	5.85
Er	150	0.35	0.29	0.83	5.63
Yb	99	0.31	0.26	0.84	5.50
Ho	60	0.11	0.088	0.80	5.74
Tb	56	0.061	0.044	0.72	5.96
Eu	31	0.025	0.015	0.60	6.09
Tm	18	0.049	0.040	0.82	5.57
Lu	15	0.055	0.049	0.89	5.46

The enrichment factor k_e demonstrates the efficient removal of manganese from the water phase, indicating high affinity for incorporation in the precipitating YBS, and also for iron (similar charge and size as for manganese), as well as the light REEs (LREEs). Lower enrichment factors are observed for copper, zinc, barium, vanadium, and yttrium, as well as the heavy REEs (HREEs). The behavior of yttrium is similar to the heaviest of HREEs, as expected for charge- and radius-controlled behavior (CHARAC) [48]. Zinc, copper, and vanadium, however, exhibit higher enrichment than expected, considering charge and size. The enrichment of REE is highest for cerium and decreasing with increasing atomic number. The strong enrichment of cerium may be due to oxidation of Ce(III) to Ce(IV). Oxidation of Ce(III) by Mn(IV) has previously been reported, and the oxidation processes have been discussed with examples from other Mn-oxide systems [27,29,48–54].

The differences in concentrations of the trace elements between Aq_A and Aq_B (sampled within 1 h on the same day) indicate a progressive formation of the biogenic YBS phase. This is illustrated by the distribution of the elements in the water phase, Figure 4, showing the depletion as a function of ionic radii, using data from Table 1. This is evidently a dynamic process leading to changes in concentrations in a time span of hours, or less. The depletion is increasing with increasing radii for the REE. There is no evident depletion for aluminum and strontium among the trace elements. The composition of YBS species is given in Table 2: original YBS before washing (YBS_{Nat}); after sequential washing (YBS_{Red}); and after exposure to sodium, calcium, lanthanum, and iron solutions, respectively (YBS_{Na} , YBS_{Ca} , YBS_{La} , and YBS_{Fe}).

Table 2. YBS composition (mg/kg) for the YBS varieties. Same elements as in Table 1.

Element	YBS_{Nat} mg/kg	YBS_{Red} mg/kg	YBS_{Na} mg/kg	YBS_{Ca} mg/kg	YBS_{La} mg/kg	YBS_{Fe} mg/kg
Mn(III,IV)	452,710	528,230	507,030	486,120	537,290	483,340
M(I)						
Na	399	1823	19,265	73	69	84
K	666	1310	1109	1255	437	372
M(II)						
Ca	64,170	57,930	68,067	104,270	10,723	8640
Mg	4075	2442	1826	1405	1250	700
Ba	1765	1959	1856	1817	2199	1250
Cu	1555	1838	1716	1652	1727	1035
Sr	639	707	627	504	178	45
Zn	276	237	224	204	232	81
M(III)						
Y	1357	1515	1430	1350	909	372
Al	841	850	1208	925	693	532
V	683	664	627	591	630	605
Fe	583	666	1424	707	533	95,931
REE						
Ce	3180	3121	2946	2785	2928	2203
La	1825	1634	1549	1474	124,315	497
Nd	1785	1685	1592	1499	984	516
Gd	419	419	394	377	291	137
Pr	418	403	383	363	220	122
Sm	375	369	347	329	239	121
Dy	308	335	329	303	230	103
Er	150	171	162	155	118	51
Yb	99	116	110	106	90	38
Ho	60	65	61	58	45	20
Tb	56	65	60	60	42	19
Eu	31	31	30	28	20	10
Tm	18	21	20	19	16	7
Lu	15	17	16	16	13	6

The sequential leaching (steps C1–C3) is assumed to have removed the organic fraction, as well as exchangeable ions not needed for the charge balance, and most of the suspended and colloidal silicates. Concentrations of most of the elements in YBS_{Red} are higher than in YBS_{Nat} since a significant fraction of the YBS mass has been removed. Concentrations of calcium and magnesium are lower, which may indicate losses during washing, possibly of carbonate species. The compositions of the modified YBS species, assuming a birnessite structure, $M_x[Mn(III,IV)]_2O_4 \cdot (H_2O)_n$, are given in Table 3. The stoichiometries of YBS_{Nat} and YBS_{Red} are similar, despite the fact that a significant fraction of the total mass, including minerals not associated with the birnessite phase, has been removed from YBS_{Nat} in the sequential washing process. The dominating metal (M) is calcium, followed by magnesium and REE + yttrium.

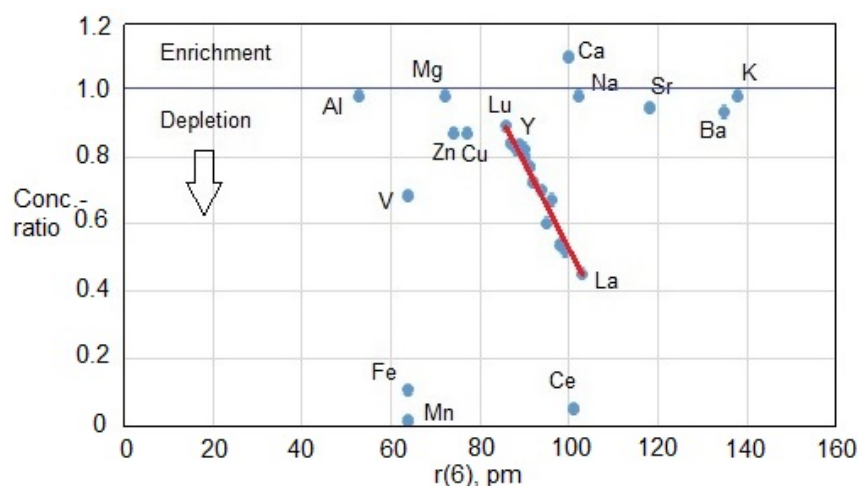


Figure 4. Metal enrichment/depletion in the fracture water. Concentration ratio $[AqB]/[AqA]$ vs ionic radii, assuming coordination number 6 (Table 3). For Ce, expected to be tetravalent, the position in the diagram may be shifted corresponding to coordination number related to ionic radii other than the assumed $r(6)$.

Table 3. Assessed birnessite composition. M and x in $M_x[Mn(III,IV)]_2O_4 \cdot (H_2O)_n$ and the effective ionic radii $r(6)$ for coordination number 6 [47]. Same elements as in Table 1, except Dy-Lu: $x < 0.001$.

Element	YBS _{Nat} x	YBS _{Red} x	YBS _{Na} x	YBS _{Ca} x	YBS _{La} x	YBS _{Fe} x	r(6) pm
Mn(III,IV)	2	2	2	2	2	2	64, 46
M(I)							
Na	0.004	0.016	0.182	0.001	0.001	0.001	102
K	0.004	0.007	0.006	0.007	0.006	0.002	138
M(II)							
Ca	0.388	0.301	0.368	0.588	0.179	0.049	100
Mg	0.040	0.021	0.016	0.013	0.012	0.007	72
Ba	0.003	0.003	0.003	0.003	0.003	0.002	135
Cu	0.006	0.006	0.006	0.006	0.006	0.004	73
Sr	0.002	0.002	0.001	0.001	0.001	<0.001	118
Zn	0.001	<0.001	0.001	0.001	0.001	<0.001	74
M(III)							
Y	0.004	0.004	0.004	0.003	0.002	0.001	90
Al	0.007	0.007	0.010	0.008	0.005	0.005	53
V	0.003	0.003	0.003	0.003	0.003	0.003	64, 59 ^a
Fe	0.003	0.003	0.006	0.003	0.002	0.391	64, 78 ^b
REE							
Ce	0.005	0.005	0.005	0.005	0.004	0.004	101, 87 ^c
La	0.002	0.002	0.002	0.002	0.183	0.001	103
Nd	0.002	0.002	0.002	0.002	0.001	0.001	98
Gd	0.001	0.001	0.001	0.001	<0.001	<0.001	94
Pr	0.001	0.001	0.001	0.001	<0.001	<0.001	99
Sm	0.001	0.001	0.001	0.001	<0.001	<0.001	96

^a V(IV). ^b Fe(II). ^c Ce(IV).

Exposure to sodium, calcium, lanthanum, and iron solutions led to corresponding changes of the proportions of cations (M), which are summarized in Table 4. Calcium is still the dominating exchangeable cation after exposure to 1 mol/L sodium solution, but calcium is partly exchanged by lanthanum. Iron is deviating from the others, which, in principle, could indicate the formation of a new phase. Fractions of the metals M in the assumed birnessite structure may be merely adsorbed on outer surfaces of the oxide phase (besides the dissolution of carbonates and hydroxides present in the natural YBS). However,

exchange capacities below 10 meq/kg were reported for a selection of oxides (pyrolusite, hematite, magnetite, limonite, and gibbsite with particle sizes 0.044–0.063 mm; surface area ca. 2 m²/g for pyrolusite) in the pH range 7–9 [55], based on measurements by an isotopic dilution technique [56]. This may indicate that only a minor fraction of the major elements M would be adsorbed on outer-sphere positions. The effects of exposure of YBS_{Red} to high concentrations of sodium and calcium on the levels of the trace elements (copper and zinc, as well as Y + REE, Table 4) are minor, which indicate that these elements are bound to the birnessite phase in inner-sphere, rather than outer-sphere, positions and are not readily exchangeable. An assumption—however, not verified experimentally—is that there is a charge balance; the positive charges of M_x and the Mn(III)/Mn(IV) ratio correspond to the negative charge from O₄.

Table 4. Assessed birnessite composition. M and x in M_x[Mn(III,IV)]₂O₄·(H₂O)_n; elements with x = 0.01 or higher. Blank: <0.01.

Element M	YBS _{Nat} x	YBS _{Red} x	YBS _{Na} x	YBS _{Ca} x	YBS _{La} x	YBS _{Fe} x
Na		0.02	0.18			
Ca	0.39	0.30	0.37	0.59	0.18	0.05
Mg	0.04	0.02	0.02	0.01	0.01	0.01
Fe			0.01			0.39
REE + Y	0.02	0.02	0.02	0.01	0.19	0.01
ΣOthers, x <0.01	0.03	0.03	0.03	0.03	0.03	0.02
Σx	0.48	0.39	0.63	0.64	0.41	0.48

Uptake of europium by birnessite in inner-sphere positions, independently of pH, has previously been reported [57]. The differences between outer-sphere and inner-sphere adsorption are discussed in some detail by Appelo and Postma (1999) [20], as well as by Kwon et al. (2013) [58].

3.3. Phase Analysis

X-Ray diffractograms are given in Figure 5. The peaks, denoted A–R in the figure, were determined using the PANalytical HighScore software.

Four distinct peaks from 7 Å manganates/birnessite (comparison with birnessite reference sample ICSD, reference code 98-015-2288) were present in all of the YBS samples (2 Theta within parenthesis): B—7.3–7.5 Å (11.8–12.2); E—3.6–3.7 Å (24.2–24.5); J—2.45–2.46 Å (36.6–36.7); T—1.41–1.42 Å (66). Two peaks may indicate the presence of a fraction of 10 Å manganates/todorokite with the composition M_x[Mn(III,IV)]₆O₁₂·(H₂O)_{3–4.5}. M is usually calcium, sodium, and potassium with x around 2, i.e., A—8.7–8.9 Å (8–9), C—4.9 Å (17–18), not for YBS_{Fe} and YBS_{La}. For all of the samples, there was a diffuse peak area corresponding to ca. 1.7 Å (50–55), not identified.

Silicates and calcite in YBS_{Nat} (D, F–H, I, K–O) were reduced or absent in YBS_{Red}, which indicates and confirms that the sequential washing process was efficient in removing trace minerals, like feldspars, quartz, and carbonates, besides amorphous phases and adsorbates. No discrete iron phase was indicated in YBS_{Nat} or in YBS_{Red}.

There are a minimum of 50 reported structure analyses of synthetic birnessite, but also some on natural birnessite, generally of biogenic origin (e.g., [5,6,10,15,40,51,59–63]). Almost all studies identify the four peaks B, E, J, and R as being characteristic of hexagonal birnessite. Biological tissue, if present, would generate a peak in the area of E [10,61,62]. Saturation of a synthetic Na-birnessite with several metals, including calcium and lanthanum, is reported by Golden et al. (1987) [64]. XRD patterns indicate a difference, with a peak at 3.56 Å, in the La-birnessite, not present in the Ca-birnessite. A similar difference between YBS_{La} and YBS_{Ca} was, however, not observed (cf. peak E).

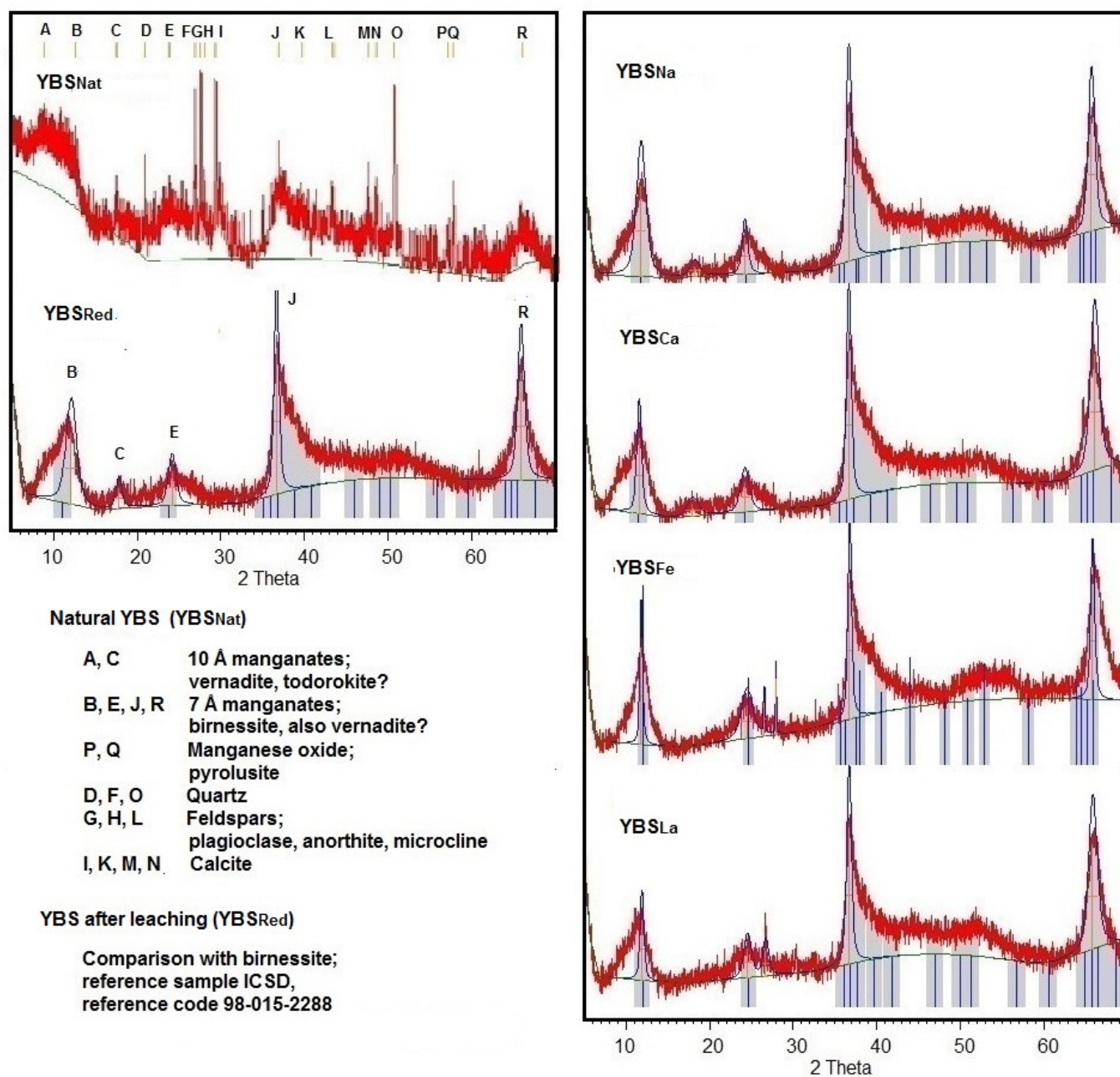


Figure 5. X-ray diffractograms. Natural YBS (YBS_{Nat}), YBS after leaching (YBS_{Red}), and YBS after exposure to 1 M Na, Ca, Fe, and La solutions, respectively (YBS_{Na}, YBS_{Ca}, YBS_{La}, and YBS_{Fe}).

3.4. Infrared Spectroscopy

FTIR spectra of YBS species are given in Figure 6. IR spectra of solid birnessite have been reported, e.g., [7,28,30,38,39,41,57,64–72]. The peaks around 3400 cm⁻¹ and 1610 cm⁻¹ correspond to OH-stretching and H₂O-bending, respectively [7,39,68,69]. Peaks around 1085–1150 cm⁻¹ correspond to Mn–O-stretching [66,68], as well as peaks generally below 800–900 cm⁻¹ [7,41]. The presence of Mn(III) can be verified in YBS, but the differences between the spectra are minor and not conclusive with respect to the differences in structure or composition of the various YBS phases.

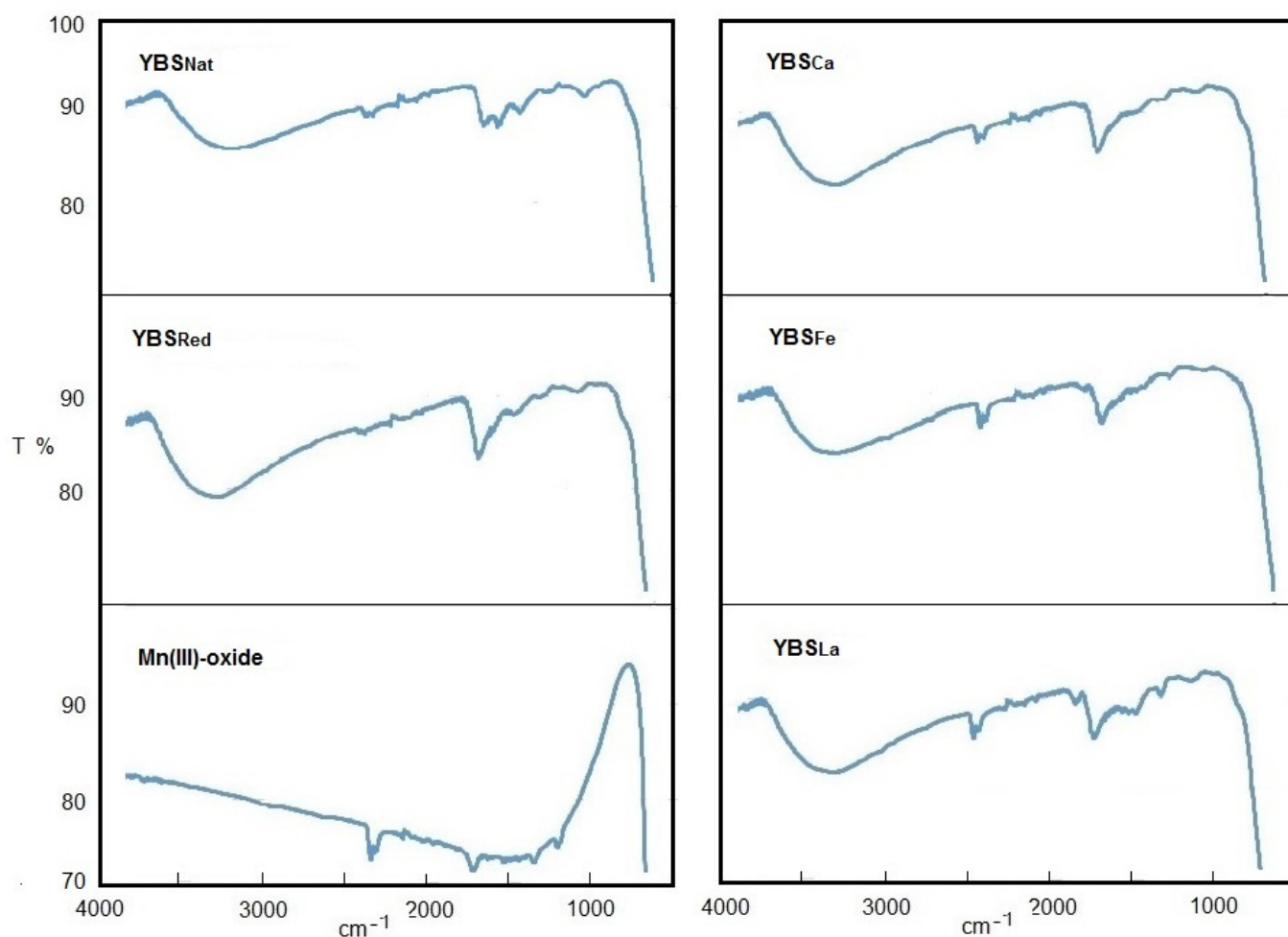


Figure 6. IR transmittance spectra of solid YBS and a Mn(III) reference, $Mn_2O_3(s)$.

4. Conclusions

It was confirmed that the formation and precipitation of birnessite in the Ytterby mine tunnel is a fast, active process, as assessed already in [45]. Favorable conditions for the formation of microbially induced REE-enriched birnessite deposits are evidently provided in Ytterby mine by (1) the continuous supply of reduced Mn, as well as REEs, by the fracture water; (2) a well-buffered system keeping the pH stable, slightly above circumneutral; and possibly also (3) the sharp redox boundary between the anoxic environment in the water-bearing bedrock fractures and the oxygenated tunnel.

The composition of the birnessite reflects the presence of metals of suitable charge and size in the water phase, notably, sodium, calcium, and Y + REE. There is a strong preference for trivalent over divalent and monovalent ions in the structure for ions of similar size. The exchange of cations (sodium, calcium, lanthanum, iron) had no apparent effect on the birnessite structure. There is a suitable cation size, with an ionic radius around 90–100 pm (sodium, calcium, and Y + REE), but also, metals with a radius around 65–75 pm (copper, zinc, vanadium, and iron) appear to be part of the birnessite structure. Cations of proper size and charge in the water are most likely bound to the manganese oxide in inner-sphere positions, between the Mn-O planes, but a minor fraction may also be adsorbed on the outer surfaces, but not affecting the phase structure.

Iron that would be trivalent under the present redox conditions is not forming a separate detectable discrete mineral phase that could be identified in the XRD phase analysis. The radii of Fe(III) and Mn(III) are almost identical (around 64 pm), and an exchange with Mn(III) in the structure can not a priori be dismissed (almost identical size,

charge, and coordination properties). There is also a cerium anomaly, most likely due to oxidation of Ce(III) to Ce(IV), leading to higher enrichment of cerium than expected for the trivalent state.

Author Contributions: Conceptualization, B.A. and S.S.; methodology, B.A., S.S., V.S., and H.S.; software, S.S., V.S., and H.S.; validation, B.A., S.S., and V.S.; formal analysis, B.A. and S.S.; investigation, B.A. and S.S.; resources, S.S., H.S., and S.K.; data curation, B.A., S.S., and V.S.; writing—original draft preparation, B.A. and S.S.; writing—review and editing, B.A. and S.S.; visualization, B.A. and S.S.; supervision, B.A.; project administration, S.S. and S.K.; funding acquisition, B.A., S.S., and S.K. All authors have read and agreed to the published version of the manuscript.

Funding: This research received no external funding, except for laboratory support from the faculty (Stockholm University and Örebro University).

Data Availability Statement: Data supporting the presented results are available by contacting the corresponding author.

Acknowledgments: The Swedish Fortification Authority allowed access to the Ytterby mine, which is gratefully acknowledged, as well as the assistance by P-O Lundgren (The Swedish Defence) and Martin Lundmark and Annika Agneson (The Swedish Fortification Agency) during sampling campaigns. Advice and continuous support from Christophe Dupraz and Rolf Hallberg have been of great help. The project is a collaboration among research groups at Stockholm University, Örebro University, and the Swedish Museum of Natural History. Access to laboratory facilities, as well as technical assistance, is gratefully acknowledged.

Conflicts of Interest: The authors declare no conflict of interest. The funders had no role in the design of the study; in the collection, analyses, or interpretation of data; in the writing of the manuscript; or in the decision to publish the results.

References

1. Sjöberg, S.; Allard, B.; Rattray, J.E.; Callac, N.; Grawunder, A.; Ivarsson, M.; Sjöberg, V.; Karlsson, S.; Skelton, A.; Dupraz, C. Rare earth element enriched birnessite in water-bearing fractures, the Ytterby mine, Sweden. *Appl. Geochem.* **2017**, *78*, 158–171. [[CrossRef](#)]
2. Nordenskjöld, I. Der Pegmaitite von Ytterby. *Bull. Geol. Inst. Univ. Uppsala* **1910**, *IX*, 1908–1909.
3. Sundius, N. *Description of the Bedrock Map of the Stockholm Region*; Sveriges Geologiska Undersökning, Ser. Ba No: 13, Kungl. Boktryckeriet. P.A; Norstedt & Söner: Stockholm, Sweden, 1948. (In Swedish)
4. Ma, X.; Ralph, J.; Zhang, J.; Que, X.; Prabhu, A.; Morrison, S.M.; Hazen, R.M.; Wyborn, L.; Lehnert, K. OpenMindat: Open and FAIR mineralogy data from the Mindat database. *Geosci. Data J.* **2023**, *1*–11. [[CrossRef](#)]
5. Jones, L.H.P.; Milne, A.A. Birnessite, a new manganese oxide mineral from Aberdeenshire, Scotland. *Miner. Mag.* **1956**, *31*, 283–288. [[CrossRef](#)]
6. Glover, E.D. Characterization of a marine birnessite. *Am. Mineral.* **1977**, *62*, 278–285.
7. Potter, R.M.; Rossman, G.R. The tetravalent manganese oxides: Identification, hydration, and structural relationships by infrared spectroscopy. *Am. Mineral.* **1979**, *64*, 1199–1218.
8. Drits, V.A.; Silvester, E.; Gorshkov, A.I.; Manceau, A. Structure of synthetic monoclinic Na-rich birnessite and hexagonal birnessite: I. Results from X-ray diffraction and selected-area electron diffraction. *Am. Miner.* **1997**, *82*, 946–961. [[CrossRef](#)]
9. Tebo, B.M.; Bargar, J.R.; Clement, B.G.; Dick, G.J.; Murray, K.J.; Parker, D.; Verity, R.; Webb, S.M. Biogenic manganese oxides: Properties and mechanisms of formation. *Annu. Rev. Earth Planet Sci.* **2004**, *32*, 287–328. [[CrossRef](#)]
10. Villalobos, M.; Lanson, B.; Manceau, A.; Toner, B.; Sposito, G. Structural model for biogenic Mn oxide produced by *Pseudomonas putida*. *Am. Mineral.* **2006**, *91*, 489–502. [[CrossRef](#)]
11. Bargar, J.R.; Fuller, C.C.; Marcus, M.A.; Brearley, A.J.; De la Rosa, M.P.; Webb, S.M.; Caldwell, W.A. Structural characterization of terrestrial microbial Mn oxides from Pinal Creek, AZ. *Geochim. Cosmochim. Acta* **2009**, *73*, 889–910. [[CrossRef](#)]
12. Dick, G.J.; Clement, B.G.; Webb, S.M.; Fodrie, F.J.; Bargar, J.R.; Tebo, B.M. Enzymatic microbial Mn(II) oxidation and Mn biooxide production in the Guyamas Basin deep-sea hydrothermal plume. *Geochim. Cosmochim. Acta* **2009**, *73*, 6517–6530. [[CrossRef](#)]
13. Pena, J.; Kwon, K.D.; Refson, K.; Bargar, J.R.; Sposito, G. Mechanisms of nickel sorption by a bacteriogenic birnessite. *Geochim. Cosmochim. Acta* **2010**, *74*, 3076–3089. [[CrossRef](#)]
14. Spiro, T.G.; Bargar, J.R.; Sposito, G.; Tebo, B.M. Bacteriogenic manganese oxides. *Accounts Chem. Res.* **2010**, *43*, 2–9.
15. Santelli, C.M.; Webb, S.M.; Dohnalkova, A.C.; Hansel, C.M. Diversity of Mn oxides produced by Mn(II)-oxidizing fungi. *Geochim. Cosmochim. Acta* **2011**, *75*, 2762–2776. [[CrossRef](#)]

16. Allard, S.; Gutierrez, L.; Fontaine, C.; Croue, J.-P.; Gallard, H. Organic matter interactions with natural manganese oxide and synthetic birnessite. *Sci. Total Environ.* **2017**, *583*, 487–495. [[CrossRef](#)]
17. Post, J.E.; Veblen, D.R. Crystal structure determinations of synthetic sodium, magnesium, and potassium birnessite using TEM and the Rietveld method. *Am. Miner.* **1990**, *75*, 477–489.
18. Drits, V.A.; Lanson, B.; Gorshkov, A.I.; Manceau, A. Substructure and superstructure of four-layer Ca-exchanged birnessite. *Am. Mineral.* **1998**, *83*, 97–118. [[CrossRef](#)]
19. Silvester E Manceau, A.; Drits, V.A. Structure of synthetic Na-rich birnessite and hexagonal birnessite: II. Results from chemical studies and EXAFS spectroscopy. *Am. Mineral.* **1997**, *82*, 962–978. [[CrossRef](#)]
20. Appelo, C.A.J.; Postma, D. A consistent model for surface complexation on birnessite ($-\text{MnO}_2$) and its application to a column experiment. *Geochim. Cosmochim. Acta* **1999**, *63*, 3039–3304. [[CrossRef](#)]
21. Lanson, B.; Drits, V.A.; Feng, Q.; Manceau, A. Structure of triclinic Na-rich birnessite. *Acta Cryst.* **2000**, *A56*, 366. [[CrossRef](#)]
22. Lanson, B.; Drits, V.A.; Gaillot, A.C.; Silvester, E.J.; Plancon, A.; Manceau, A. Structure of heavy-metal sorbed birnessite: Part 1. Results from X-ray diffraction. *Am. Mineral.* **2002**, *87*, 1631–1645. [[CrossRef](#)]
23. Drits, V.A.; Lanson, B.; Bougerol-Chaillout, C.; Gorshkov, A.I.; Manceau, A. Structure of heavy-metal sorbed birnessite. Part 2: Results from electron diffraction. *Am. Mineral. Soc. Am.* **2002**, *87*, 1646–1661.
24. Post, J.E.; Heaney, P.J.; Hanson, J. Rietveld refinement of a triclinic structure for synthetic Na-birnessite using synchrotron powder diffraction data. *Powder Diffract.* **2002**, *17*, 218–221. [[CrossRef](#)]
25. Gaillot, A.-C.; Flot, D.; Drits, V.A.; Manceau, A.; Burghammer, M.; Lanson, B. Structure of synthetic K-rich birnessite obtained by high-temperature decomposition of KMnO_4 . I. Two-layer polytype from 800C experiment. *Chem. Mater.* **2003**, *15*, 4666–4678. [[CrossRef](#)]
26. Villalobos, M.; Toner, B.; Bargar, J.; Sposito, G. Characterization of the manganese oxide produced by *Pseudomonas putida* strain MnB1. *Geochim. Cosmochim. Acta* **2003**, *67*, 2649–2662. [[CrossRef](#)]
27. Davranche, M.; Pourret, O.; Gruau, G.; Dia, A.; Le Coz-Bouhnik Caren, M. Adsorption of REE(III)-humate complexes onto MnO_2 : Experimental evidence for cerium anomaly and lanthanide tetrad effect suppression. *Geochim. Cosmochim. Acta* **2005**, *69*, 4825–4834. [[CrossRef](#)]
28. Feng, X.H.; Tan, W.F.; Liu, F.; Huang, Q.; Liu, X. Pathways of birnessite formation in alkali medium. *Sci. China Ser. D Earth Sci.* **2005**, *48*, 1438–1451. [[CrossRef](#)]
29. Davranche, M.; Pourret, O.; Gruau, G.; Dia, A.; Jin, D.; Gaertner, D. Competitive binding of REE to humic acid and manganese oxide: Impact of reaction kinetics on development of cerium anomaly and REE adsorption. *Chem. Geol.* **2008**, *247*, 154–170. [[CrossRef](#)]
30. Johnson, E.A.; Post, J.E. Water in the interlayer region of birnessite: Importance in cation exchange and structural stability. *Am. Mineral.* **2006**, *91*, 609–618. [[CrossRef](#)]
31. Lopano, C.L.; Heaney, P.J.; Post, J.E.; Hanson, J.; Komarneni, S. Time-resolved structural analysis of K- and Ba-exchange reactions with synthetic Na-birnessite using synchrotron X-ray diffraction. *Am. Miner.* **2007**, *97*, 380–387. [[CrossRef](#)]
32. Lopano, C.L.; Heaney, P.J.; Post, J. Cs-exchange in birnessite: Reaction mechanisms inferred from time-resolved X-ray diffraction and transmission electron microscopy. *Am. Mineral.* **2009**, *94*, 816–826. [[CrossRef](#)]
33. Kang, K.C.; Ju, J.H.; Kiim, S.S.; Baik, M.H.; Rhee, S.W. Sorption of aqueous Pb^{2+} ion on synthetic manganese oxides-intercalated with exchangeable cations. *J. Industr. Eng. Chem.* **2011**, *17*, 565–569. [[CrossRef](#)]
34. Cygan, R.T.; Post, J.E.; Heaney, P.J.; Kubick, J.D. Molecular models of birnessite and related hydrated layered minerals. *Amer. Mineral.* **2012**, *97*, 1505–1514. [[CrossRef](#)]
35. Wang, Y.; Feng, X.; Villalobos, M.; Tan, W.; Liu, F. Sorption behaviour of heavy metals on birnessite: Relationship with its Mn average oxidation state and implications for types of sorption sites. *Chem. Geol.* **2012**, *292–293*, 25–34. [[CrossRef](#)]
36. Yin, H.; Tan, W.; Zheng, L.; Cui, H.; Qiu, G.; Liu, F.; Feng, X. Characterization of Ni-rich hexagonal birnessite and its geochemical effects on aqueous $\text{Pb}^{2+}/\text{Zn}^{2+}$ and As(III). *Geochim. Cosmochim. Acta* **2012**, *93*, 47–62. [[CrossRef](#)]
37. Yin, H.; Liu, F.; Feng, X.; Hu, T.; Zheng, L.; Qui, G.; Koopal, L.K.; Tan, W. Effects of Fe doping on the structures and properties of hexagonal birnessites—Comparison with Co and Ni doping. *Geochim. Cosmochim. Acta* **2013**, *117*, 1–15. [[CrossRef](#)]
38. Boumaiza, H.; Coustel, R.; Medjahdi, G.; Ruby, C.; Bergaoui, L. Conditions for the formation of pure birnessite during the oxidation of Mn(II) cations in aqueous alkaline medium. *J. Solid State Chem.* **2017**, *248*, 18–25. [[CrossRef](#)]
39. White, W.B.; Vito, C.; Scheetz, E. The mineralogy and trace element chemistry of black manganese oxide deposits from caves. *J. Cave Karst Studies* **2009**, *71*, 136–143.
40. Frierdich, A.J.; Hasenmueller, E.A.; Catalano, J.G. Composition and structure of nanocrystalline Fe and Mn oxide cave deposits: Implications for trace element mobility in karst systems. *Chem. Geol.* **2011**, *284*, 82–96. [[CrossRef](#)]
41. Miller, A.Z.; Dionisio, A.; Sequeira Braga, M.A.; Hernandez-Mariné, M.; Afonso, M.J.; Muralha, V.S.F.; Herrera, L.K.; Raabe, J.; Fernandez-Cortes, A.; Cuezva, S.; et al. Biogenic Mn oxide minerals coating in a subsurface granite environment. *Chem. Geol.* **2012**, *322–323*, 181–191. [[CrossRef](#)]
42. Sjöberg, S. Microbially Mediated Manganese Oxides Enriched in Yttrium and Rare Earth Elements in the Ytterby Mine. Ph.D. Thesis, Stockholm University, Stockholm, Sweden, 2019.
43. Sjöberg, S.; Callac, N.; Allard, B.; Smittenberg, R.H.; Dupraz, C. Microbial communities inhabiting a rare earth element enriched birnessite-type manganese deposit in the Ytterby mine, Sweden. *Geomicrobiol. J.* **2018**, *35*, 657–674. [[CrossRef](#)]

44. Sjöberg, S.; Stairs, C.; Allard, B.; Hallberg, R.; Homa, F.; Martin, T.; Ettema, T.J.G.; Dupraz, C. Bubble biofilm: Bacterial colonization of air-air interface. *Biofilm* **2020**, *2*, 100030. [[CrossRef](#)]
45. Sjöberg, S.; Stairs, C.; Allard, B.; Homa, F.; Martin, T.; Sjöberg, V.; Ettema, T.J.G.; Dupraz, C. Microbiomes in a manganese oxide producing ecosystem in the Ytterby mine, Sweden: Impact on metal mobility. *FEMS Microbiol. Ecol.* **2020**, *96*, 11. [[CrossRef](#)] [[PubMed](#)]
46. Sjöberg, S.; Yu, C.; Stairs, C.W.; Allard, B.; Hallberg, R.; Henriksson, S.; Åström, M.; Dupraz, C. Microbe-Mediated Mn Oxidation—A Proposed Model of Mineral Formation. *Minerals* **2021**, *11*, 1146. [[CrossRef](#)]
47. Aylward, G.; Findlay, T. *SI Chemical Data*, 5th ed.; John Wiley and Sons: Melbourne, Australia, 2002.
48. Bau, M.; Koschinsky, A. Oxidative scavenging of cerium on hydrous Fe oxide: Evidence from the distribution of rare earth elements and yttrium between Fe oxides and Mn oxides in hydrogenetic ferromanganese crusts. *Chem. Geol.* **2009**, *43*, 37–47.
49. De Carlo, E.H.; Wen, X. The influence of redox reactions on the uptake of dissolved Ce by suspended Fe and Mn oxide particles. *Aquat. Geochem.* **1998**, *3*, 357–389. [[CrossRef](#)]
50. Ohta, A.; Kawabe, I. REE(III) adsorption onto Mn dioxide (δ -MnO₂) and Fe oxyhydroxide: Ce(III) oxidation by δ -MnO₂. *Geochim. Cosmochim. Acta* **2001**, *65*, 695–703. [[CrossRef](#)]
51. Tanaka, K.; Tani, Y.; Takahashi, Y.; Tanimizu, M.; Suzuki, Y.; Kozai, N.; Ohnuki, T. A specific Ce oxidation process during sorption of rare earth elements on biogenic Mn oxide produced by *Acremonium* sp. Strain KR21-2. *Geochim. Cosmochim. Acta* **2010**, *74*, 5463–5477. [[CrossRef](#)]
52. Loges, A.; Wagner, T.; Barth, M.; Bau, M.; Göb, S.; MArkl, G. Negative Ce anomalies in Mn oxides: The role of Ce⁴⁺ mobility during water-mineral interaction. *Geochim. Cosmochim. Acta* **2012**, *86*, 296–317. [[CrossRef](#)]
53. Ohnuki, T.; Jiang, M.; Sakamoto, F.; Kozai, N.; Yamasaki, S.; Yu, Q.; Tanaka, K.; Utsumomiya, S.; Xia, X.; Yang, K.; et al. Sorption of trivalent cerium by a mixture of microbial cells and manganese oxides: Effect of microbial cells on the oxidation of trivalent cerium. *Geochim. Cosmochim. Acta* **2015**, *163*, 1–13. [[CrossRef](#)]
54. Kraemer, D.; Tepe, N.; Pourret, O.; Bau, M. Negative cerium anomalies in manganese (hydr)oxide precipitates due to cerium oxidation in the presence of dissolved siderophores. *Geochim. Cosmochim. Acta* **2017**, *196*, 197–208. [[CrossRef](#)]
55. Allard, B.; Karlsson, M.; Tullborg, E.-L.; Larson, S.Å. *Ion Exchange Capacities and Surface Areas of Some Major Components and Common Fracture Filling Materials of Igneous Rocks*; SKBF Technical Report 83-64; Swedish Nuclear Fuel Supply Co/Division KBS: Stockholm, Sweden, 1983.
56. Francis, C.W.; Grigal, D.F. A rapid and simple procedure using Sr⁸⁵ for determining cation exchange capacities of soils and clays. *Soil. Sci.* **1971**, *112*, 17–21. [[CrossRef](#)]
57. Dong, L.; Liao, Q.; Linghu, W.; Huang, Y.; Shen, R.; Alsaedi, A.; Wang, J.; Hayar, Y.T.; Sheng, G. Application of EXAFS with a bent crystal analyzer to study the pH-dependent microstructure of Eu(III) onto birnessite. *J. Environ. Chem. Eng.* **2018**, *6*, 842–848. [[CrossRef](#)]
58. Kwon, K.D.; Refson, K.; Sposito, G. Understanding the trends in transition metal sorption by vacancy sites in birnessite. *Geochim. Cosmochim. Acta* **2013**, *101*, 222–232. [[CrossRef](#)]
59. Saratovsky, I.; Wightman, P.G.; Pasten, P.A.; Gaillard, J.-F.; Poeppelmeier, K.R. Manganese oxides: Parallels between abiotic and biotic structures. *J. Am. Chem. Soc.* **2006**, *128*, 11188–11198. [[CrossRef](#)] [[PubMed](#)]
60. Saratovsky, I.; Gurr, S.J.; Hayward, M.A. The structure of manganese oxide formed by the fungus *Acremonium* sp. Strain KR21-2. *Geochim. Cosmochim. Acta* **2009**, *73*, 3291–3300. [[CrossRef](#)]
61. Yu, Q.; Sasaki, K.; Tanaka, K.; Ohnuki, T.; Hirajima, T. Structural factors of biogenic birnessite produced by fungus *Paraconiothyrium* sp. WL-2 strain affecting sorption of Co²⁺. *Chem. Geol.* **2012**, *310–311*, 106–113. [[CrossRef](#)]
62. Yu, Q.; Sasaki, K.; Tanaka, K.; Ohnuki, T.; Hirajima, T. Zinc sorption during bio-oxidation and precipitation of manganese modifies the layer stacking of biogenic birnessite. *Geomicrobiol. J.* **2013**, *30*, 829–839. [[CrossRef](#)]
63. Mayanna, S.; Peacock, C.L.; Schaffner, F.; Grawunder, A.; Merten, D.; Kothe, E.; Buchel, G. Biogenic precipitation of manganese oxides and enrichment of heavy metals at acidic soil pH. *Chem. Geol.* **2015**, *402*, 6–17. [[CrossRef](#)]
64. Golden, D.C.; Chen, C.C.; Dixon, J.B. Transformation of birnessite to buserite, todorokite, and manganite under mild hydrothermal treatment. *Clays Clay Minerals* **1987**, *35*, 271–280. [[CrossRef](#)]
65. Luo, J.; Huang, A.; Park, S.H.; Suib, S.L.; O'Young, C.-L. Crystallization of sodium-birnessite and accompanied phase transformation. *Chem. Mater.* **1998**, *10*, 1561–1568. [[CrossRef](#)]
66. Yang, D.S.; Wang, M.K. Synthesis and characterization of well-crystallized birnessite. *Chem. Mater.* **2001**, *13*, 2589–2594. [[CrossRef](#)]
67. Novikov, G.V.; Kulikova, L.N.; Bogdanova, O.Y.; Sychkova, G.I. Layered hydrous manganese dioxide saturated with alkaline-earth cations: Synthesis and sorption properties. *Russ. J. Inorg. Chem.* **2006**, *51*, 177–188. [[CrossRef](#)]
68. Kang, L.; Zhang, M.; Liu, Z.-H.; Ooi, K. IR spectra of manganese oxides with either layered or tunnel structures. *Spectrochim. Acta* **2007**, *A67*, 864–869. [[CrossRef](#)]
69. Eren, E.; Gumus, H.; Sarihan, A. Synthesis, structural characterization and Pb(II) adsorption behaviour of K- and H-birnessite samples. *Desalination* **2011**, *279*, 75–85. [[CrossRef](#)]
70. Yin, H.; Liu, F.; Feng, X.; Liu, M.; Tan, W.; Qiu, G. Co²⁺-exchange mechanism of birnessite and its application for the removal of Pb²⁺ and As(III). *J. Hazardous Mater.* **2011**, *196*, 318–326. [[CrossRef](#)]

71. Atkins, A.L.; Shaw, S.; Peacock, C.L. Nucleation and growth of todorokite from birnessite: Implications for trace metal cycling in marine sediments. *Geochim. Cosmochim. Acta* **2014**, *144*, 109–125. [[CrossRef](#)]
72. Yin, H.; Kwon, K.D.; Lee, J.-Y.; Shen, Y.; Zhao, H.; Wang, X.; Liu, F.; Zhang, J.; Feng, X. Distinct effects of Al³⁺ doping on the structure and properties of hexagonal turbostratic birnessite: A comparison with Fe³⁺ doping. *Geochim. Cosmochim. Acta* **2017**, *208*, 268–284. [[CrossRef](#)]

Disclaimer/Publisher’s Note: The statements, opinions and data contained in all publications are solely those of the individual author(s) and contributor(s) and not of MDPI and/or the editor(s). MDPI and/or the editor(s) disclaim responsibility for any injury to people or property resulting from any ideas, methods, instructions or products referred to in the content.